

Photometry from Voyager 2: Initial Results from the Neptunian Atmosphere, Satellites, and Rings

ARTHUR L. LANE, ROBERT A. WEST, CHARLES W. HORD,
ROBERT M. NELSON, KAREN E. SIMMONS, WAYNE R. PRYOR,
LARRY W. ESPOSITO, LINDA J. HORN, BRAD D. WALLIS, BONNIE J. BURATTI,
THOMAS G. BROPHY, PADMA YANAMANDRA-FISHER, JOSHUA E. COLWELL,
DAVID A. BLISS, MARVIN J. MAYO, WILLIAM D. SMYTHE

The Voyager photopolarimeter successfully accomplished its objectives for the Neptune encounter, performing measurements on the planet, several of its satellites, and its ring system. A photometric map of Neptune at 0.26 micrometer (μm) shows the planet to be bland, with no obvious contrast features. No polar haze was observed. At 0.75 μm , contrast features are observed, with the Great Dark Spot appearing as a low-albedo region and the bright companion as being substantially brighter than its surroundings, implying it to be at a higher altitude than the Great Dark Spot. Triton's linear phase coefficients of 0.011 magnitudes per degree at 0.26 μm and 0.013 magnitudes per degree at 0.75 μm are consistent with a solid-surface object possessing high reflectivity. Preliminary geometric albedos for Triton, Nereid, and 1989N2 were obtained at 0.26 and 0.75 μm . Triton's rotational phase curve shows evidence of two major compositional units on its surface. A single stellar occultation of the Neptune ring system elucidated an internal structure in 1989N1R, in the ~ 50 -kilometer region of modest optical depth. 1989N2R may have been detected. The deficiency of material in the Neptune ring system, when compared to Uranus', may imply the lack of a "recent" moon-shattering event.

WITH THE NEPTUNIAN SYSTEM AS the "last stop" on the Voyager 2 Grand Tour trajectory and successful Jupiter, Saturn, and Uranus encounters behind (1-3), the photopolarimeter (PPS) team prepared for the instrument's most active encounter. The interplanetary travel period between Uranus and Neptune was used to refine the PPS operating parameters and test for instrument responses to the lower reflected light levels anticipated for the Neptunian system. As was done before the Uranus encounter, the planned ring occultation star σ Sagittarii was reexamined for temporal stability. The preparations for Neptune were completed successfully, and we now describe the initial results from (i) the Neptune atmospheric scattering measurements, (ii) the measurements of the satellite albedos and a phase curve for Triton, and (iii) the stellar occultation of the Neptunian ring system.

The atmosphere of Neptune. The objectives of the Neptune photometry investigation include (i) measurement of the phase-angle dependence of light scattered from Neptune. Phase-angle dependence is used to derive the phase integral (the ratio of the

Bond albedo to the geometric albedo), which is a key parameter in the global heat balance, and for inferring mean particle size. (ii) Measurement of the center-to-limb behavior of the scattered light. The vertical structure of ultraviolet-absorbing haze and the optical thickness of the methane cloud can be derived from these measurements. (iii) Measurement of the spatial distribution of hazes and clouds. Information on the spatial distribution of UV-absorbing haze provides an important constraint on the nature of the process responsible for creating the stratospheric haze, and on the mean meridional circulation of the stratosphere.

We obtained both disk-integrated and spatially resolved measurements of Neptune in the near-ultraviolet (effective wavelength 0.26 μm) and near-infrared (0.75 μm) regions. The disk-integrated measurements were performed during the inbound and outbound trajectory asymptotes at phase angles of roughly 15° and 134° , respectively. Spatially resolved measurements include a full-disk raster-scan map at 13° to 15° phase angle, three north-south scans at 14° phase angle, and a series of measurements at a variety of phase angles (14° , 18° , 60° to 70° , 137° , and 158°) targeted to latitude 30°S . Polarization data that were acquired simultaneously with these measurements will be presented elsewhere (4). Analysis of our complete photometric data set will require detailed study of the instrument pointing geometry. Therefore, the atmospheres part

of this report is limited in scope. We present below a first analysis of our raster-scan maps of the planet.

The maps were generated by stepping the PPS 0.1° field-of-view across the planet in an almost uniformly spaced grid of discrete pointings that cover a rectangle containing the planet. The angular diameter of Neptune during this map sequence was 1.6° to 2.0° . The data were reduced to I/F as a function of position, where I is the intensity and πF is the incident solar flux. The absolute calibration was determined by fitting the data with model results and by requiring that the model geometric albedo agree with the albedo derived from studies using ground-based data and International Ultraviolet Explorer (IUE) data. The geometric albedo of Neptune is quite high (0.52) at 0.26 μm (5) and quite low (0.16) at 0.75 μm (6).

The images shown in Fig. 1 were generated by interpolation between the discrete pointings to fill a fine, two-dimensional grid. Neptune has no brightness features at 0.26 μm , as seen in Fig. 1. Its appearance is bland and resembles that of Uranus at that wavelength (3). Notably absent are the polar UV-absorbing hazes seen by the PPS on Jupiter and Saturn (1, 2). The data in the map can be fit, to a good approximation, with a homogeneous atmosphere model with Rayleigh scatterers (gas and very small particles) with effective single-scattering albedo of 0.97. This model also fits the Uranus data. We found that the small optical depth of stratospheric aerosols inferred by Pollack *et al.* (7) (their model US-71) produced too little scattering to be detected as a non-Rayleigh scattered component at 0.26 μm , but that the UV absorption by stratospheric haze acted to reduce the effective single-scattering albedo of the gas. Another effect that reduces the effective single-scattering albedo is Raman scattering. The effective single-scattering albedo for a pure Rayleigh-Raman scattering atmosphere of 85% H_2 + 15% He is 0.988. Aerosols are responsible for the small UV absorption in excess of the apparent absorption due to Raman scattering.

A homogeneous model does not fit the map data perfectly. A comparison of a synthetic image produced by the homogeneous model calculation with the data is also shown in Fig. 1. A small north-south asymmetry is evident in the ratio image (Fig. 1C). The stratospheric UV-absorbing haze is more abundant in the equatorial region. Latitudes southward of 30°S are best fit by the 0.97 single-scattering albedo, whereas more equatorial latitudes (30°S to 20°N) are better fit by a value of 0.96. The map does not cover high northern latitudes, which were not available at the time of the map-

A. L. Lane, R. A. West, R. M. Nelson, L. J. Horn, B. J. Buratti, B. D. Wallis, P. Yanamandra-Fisher, D. A. Bliss, M. J. Mayo, W. D. Smythe, Jet Propulsion Laboratory, California Institute of Technology, Pasadena, CA 91109.

C. W. Hord, K. E. Simmons, W. R. Pryor, L. W. Esposito, T. G. Brophy, J. E. Colwell, Laboratory of Atmospheric and Space Physics, University of Colorado, Boulder, CO 80309.

ping measurements because of the spacecraft viewing geometry.

The absence of abundant polar hazes on both Uranus and Neptune, and their prominence in the Jovian and Saturnian atmospheres, provides a means of testing models of haze production and atmospheric transport. Both photochemical and auroral processes have been proposed as primary mechanisms for aerosol formation. The primary photochemical products known to be present in the Uranian and Neptunian atmospheres (solid C_2H_2 and C_2H_6) are colorless. Some other component, possibly complex hydrocarbons produced by solid-state photochemistry formed by UV irradiation of C_2H_2 and C_2H_6 ice particles, must be invoked to account for UV absorption. Auroral bombardment can cause hydrocarbon haze formation only when particle penetration depths are sufficient to reach altitudes where methane can be found. Auroral bombardment may explain the UV dark polar hoods at Jupiter and Saturn. All active haze-formation processes on Uranus and Neptune combine to form only very optically thin stratospheric hazes.

Images obtained during the map sequence (8) show several prominent cloud features near the center of the disk at the time our field-of-view passed over that region. A

wide-angle image taken with the $0.54\text{-}\mu\text{m}$ methane filter at flight data system (FDS) time 11358.48 is shown in Fig. 1D. A low-albedo oval called the Great Dark Spot is near the center of the image. At its southern edge is a bright cloud called the bright companion. The Great Dark Spot is evident in our $0.75\text{-}\mu\text{m}$ map (Fig. 1B) as a low-albedo region (10% darker than the surrounding intensities), whereas the bright companion is about 30% brighter than its surroundings at $0.75\text{-}\mu\text{m}$. Neither of these features are seen in the $0.26\text{-}\mu\text{m}$ map (Fig. 1A). The $0.75\text{-}\mu\text{m}$ PPS filter is centered on a window region in the methane absorption spectrum, but the wide bandpass ($0.03\text{-}\mu\text{m}$) overlaps spectral regions where methane gas absorbs. The mean absorption coefficient, derived by convolving the PPS spectral response function with the methane coefficients of Giver (9) is $0.152\text{ (km-amagat)}^{-1}$. The bright companion is a high-contrast feature in the Voyager methane images (8) and is seen in ground-based methane band images obtained during the encounter (10).

We have interpreted the contrast of the bright companion as an increase in the optical depth of the methane cloud relative to surrounding regions. The methane cloud is known to have a small average optical depth of a few tenths (11). We compared a

single scan of the map that contained the bright companion with model atmospheres having various optical depths for the methane haze. Our model atmospheres contain a thin ($\tau = 0.025$ at $0.75\text{-}\mu\text{m}$) stratospheric haze (based on Uranus model), a methane haze at the 1.5-bar level, and a deeper semi-infinite cloud at the 2.5-bar level. The pressure of the deep cloud is based on measurements of the H_2 quadrupole lines (11), whereas the pressure of the methane cloud is based on recent results of the Voyager radio science (RSS) experiment (12). We adopted isotropic scattering-phase functions for the methane haze and deep cloud. The model fit the center-to-limb data for the surrounding regions if τ of the methane cloud is 0.19. The optical depth of the methane cloud in the bright companion is then 0.45. The value of 0.45 is actually a lower limit for the optical depth, as averaged over the PPS field-of-view, because the feature is barely resolved by the PPS. A plot of intensities for the data and two models are shown in Fig. 2. An optical depth increase from 0.19 to 0.45 is much smaller than typical optical depths for convective plumes on the earth, which often have τ of several tens. The bright companion is more analogous to thin cirrus than to convective cumulus. A wave associated with the Great Dark Spot may be responsible for the enhanced optical depth of the bright companion.

Geometric albedos of the satellites and the phase curve of Triton. We obtained disk-integrated brightnesses of Triton, Nereid, and 1989N2, at a variety of solar phase angles at two wavelengths ($0.26\text{-}\mu\text{m}$ and $0.75\text{-}\mu\text{m}$). From these observations we have made a preliminary determination of the geometric albedo of these planetary satellites in the manner described by Russell (13).

The disk-integrated brightnesses of Nereid and 1989N2 are consistent with these bodies having a surface of very low reflectance. There are not a sufficient number of observations of these objects to derive a phase curve from which we could determine a geometric albedo. Therefore we extrapolated the disk-integrated brightnesses of Nereid and 1989N2 to zero phase angle using a linear phase coefficient that would be expected for low albedo objects (0.03 magnitudes per degree).

Observations of Triton were made at a wide variety of solar phase angles ranging from 12° to 136° . These data will ultimately permit us to fit a full photometric model to Triton's surface. For the purpose of determining the preliminary geometric albedo for this object, we have derived a linear phase coefficient from the 27 data measurements of disk-integrated brightness that we made at solar phase angles $12^\circ < \alpha < 28^\circ$. We use

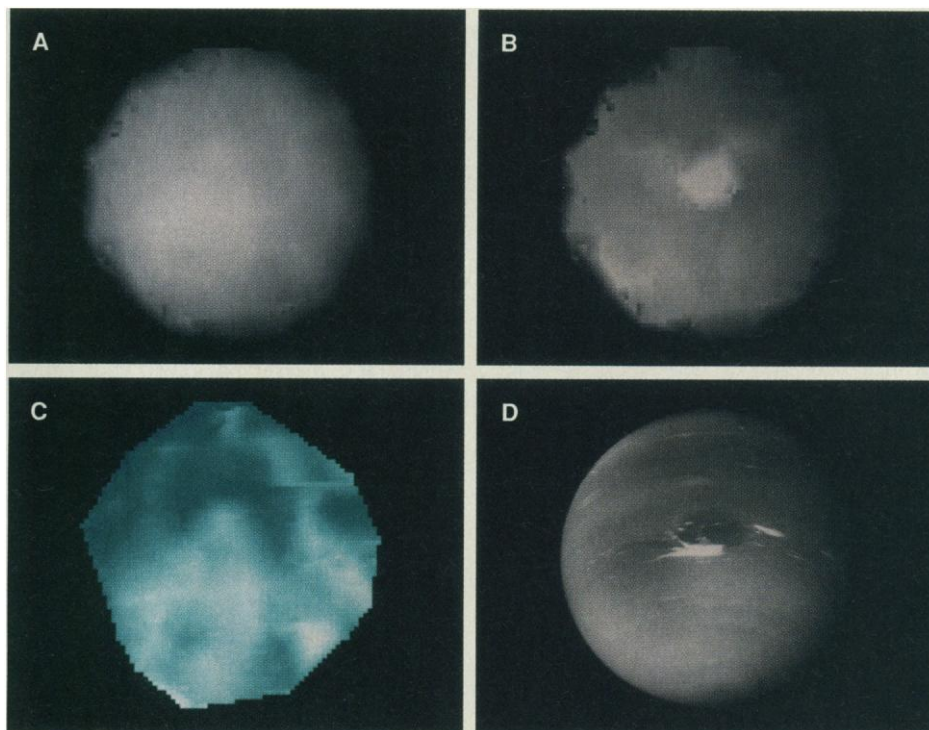


Fig. 1. (A) Neptune at $0.26\text{-}\mu\text{m}$. This 128×128 picture element image was created by interpolating in two dimensions from the raw raster-scan PPS data. (B) Neptune at $0.75\text{-}\mu\text{m}$. (C) The ratio of observed intensity, corrected for field-of-view blurring, to that for a homogeneous Rayleigh scattering model atmosphere with effective single scattering albedo 0.97. Points near the limb, where the blurring correction is large, were eliminated from the images (hence, the irregular perimeter). White regions have ratio of unity and blue regions have a ratio near 0.95. (D) Image recorded by the Voyager wide-angle camera during the map sequence. All images have the same scale and orientation (north at the top).

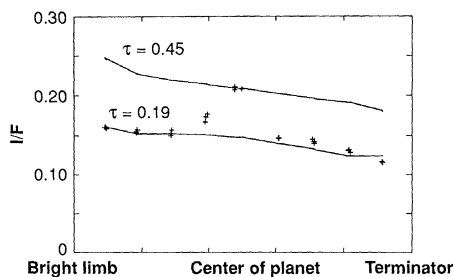


Fig. 2. I/F at $0.75 \mu\text{m}$ is shown as a function of position for a scan from the map passing through the bright companion (+). Solid curves are for model atmospheres having methane haze optical depth 0.19 and 0.45.

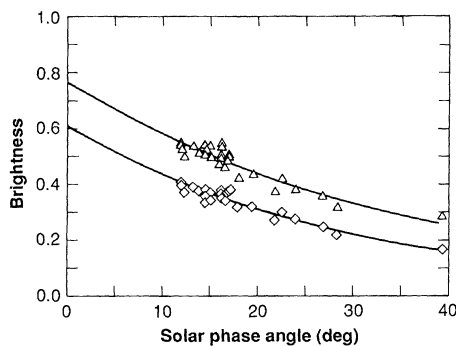


Fig. 3. Brightness variation as a function of solar phase angle for Triton. Triangles are $0.75 \mu\text{m}$ data; diamonds are $0.26 \mu\text{m}$ data. The lines represent an unweighted second order polynomial fit to each data set.

these phase coefficients and perform a linear extrapolation to zero phase to obtain the geometric albedos.

The derived linear phase coefficients for Triton are 0.011 magnitudes per degree at $0.26 \mu\text{m}$ and 0.013 magnitudes per degree at $0.75 \mu\text{m}$. The small value of these phase coefficients is consistent with linear phase coefficients derived for other solid-surface objects with high reflectivity. Generally, high-albedo objects have smaller phase coefficients than low-albedo objects because the increased importance of multiple scattering in a highly reflecting regolith fills in shadows on the surfaces. The high albedo and low phase coefficients of Triton are consistent with this generalization.

The preliminary geometric albedos we measured for Triton were 0.58 ± 0.04 and 0.74 ± 0.05 ; and for 1982N2 were 0.06 ± 0.02 and 0.07 ± 0.01 for the UV and IR filters, respectively. For Nereid the UV geometric albedo was 0.12 ± 0.03 . The IR albedo of Nereid will not be available until after the post-encounter calibration sequence is completed. For Triton we used the linear phase coefficients derived above for the purpose of extrapolating to 0° phase angle for determining the geometric albedo. For Nereid and 1989N2 we used the phase coefficients expected for similarly dark solar

system objects for this purpose. We assume radii of 1360, 170, and 95 km for Triton, Nereid, and 1989N2, respectively (8, 14). The violet and green filter geometric albedos reported by the Voyager imaging team are consistent with these results (8).

The low albedo and color ratio near unity of Nereid is consistent with a surface comprised of well-aged but reworked material. In the case of 1989N2, primordial material, possibly similar to that found on carbonaceous chondrites or redder D-type asteroids, is the most likely surface constituent. The very high albedo of Triton is consistent with a surface that has been recently renewed, such as Europa's, or a surface that may be still undergoing regeneration, such as Io's. These data are consistent with a tectonically active Triton.

The 27 observations of Triton at the UV and IR bandpasses are plotted in Fig. 3 as a function of the solar phase angle. In the figure we have fit an unweighted second-order polynomial to the data to serve a first-order approximation of a phase curve. The slope of the Triton phase curve is not as steep as that obtained by the PPS for the Uranian satellites (15). Triton's flatter phase curve is consistent with the phase behavior of bright objects that exhibit more multiple scattering.

Preliminary fits of Triton's solar-phase curve (12 to 28° phase angle) to the radiative transfer model of Hapke (16) suggest that its surface consists of particles that are slightly more backscattering than other icy satellites. This finding is unexpected in view of the fact that Triton's phase coefficient is similar to that for satellites with equivalent geometric albedos such as Europa, Mimas, and Tethys (17). This result, which needs to be corroborated by more detailed analysis, suggests that certain physical attributes of the particles comprising the regolith—such as their sizes, shapes, and indices of refraction—differ from those of other icy satellites in the outer solar system. This difference could be the result of unique crystalline or particulate structures caused by the repetitive sublimation and condensation of volatiles on Triton's surface. Such scenarios have been discussed by Trafton (18), Lunine and Stevenson (19), Stansberry (20), Zent *et al.* (21), and Stern (22).

The rotational light curves of Triton in the UV and IR filters differ markedly in their amplitudes (Fig. 4). Measurements obtained in the IR filter show very little variation as a function of geographical longitude, whereas the UV observations show that the leading side of the satellite is about 7% brighter than the trailing side. Ground-based observations demonstrate a similar correlation of the rotational light curve with

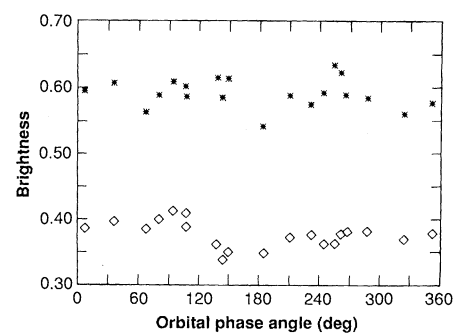


Fig. 4. Brightness variation as a function of orbital phase angle for Triton. Stars are $0.75 \mu\text{m}$ data; diamonds are $0.26 \mu\text{m}$ data. The $0.26 \mu\text{m}$ orbital phase curve indicates that the leading side of the satellite is about 7% brighter than the trailing side. The $0.75 \mu\text{m}$ data curve is flat. This result is consistent with a surface of two major compositional units: one is bright and spectrally featureless, the other is redder and concentrated mainly on the trailing side.

albedo. Franz (23) reported a 0.06 magnitude total amplitude in the astronomically defined V filter ($0.55 \mu\text{m}$), with the leading side being brighter, whereas the measurements of Lark *et al.* (24) at $0.89 \mu\text{m}$ show no variations in the lightcurve down to the 0.02 magnitude level. These results are consistent with the existence of at least two major compositional units on the surface of Triton: one is a bright, spectrally featureless component, possibly relatively pristine nitrogen or methane frost, and the other is a redder material concentrated preferentially on the trailing side. The latter material may be a compositionally distinct one, or it may be methane frost that has been preferentially altered (reddened) by an endogenic process such as interactions with energetic particles in Neptune's magnetosphere.

During departure from the Neptunian system we obtained ten observations of Triton in both filters at solar phase angles between 130° and 135° . These data are about twice as bright and measurably bluer than similar Voyager observations of icy airless bodies (15, 17, 25). We believe these measurements contain a substantial contribution from Triton's atmosphere, including light forward scattered from a haze layer. More definitive results await a detailed analysis.

Sigma Sagittarii stellar occultation of Neptune's ring system. On 24 August 1989, 5 hours before the closest flyby of Neptune, the PPS observed a stellar occultation of the Neptune ring system by the star σ Sgr. The occultation measurement was performed with the $0.26 \mu\text{m}$ UV filter and linear polarizing filter. Light from the star was sampled every 0.010 s in a manner similar to that used at Saturn and Uranus (2, 3, 26). The Neptune ring system was probed over a radial range from approximately 75,000 to 42,000 km, which includes the main region

of ring arc detections from ground-based measurements (27–29). The occultation path provided information for only a single ingress cut of a portion of the Neptune ring system. The occultation geometry is shown in Fig. 5. The radial resolution during the occultation ranged from about 80 m at the beginning of the occultation to about 10 m by the end of the occultation measurement. Using a similar methodology at Uranus, with the same star, we were able to unambiguously detect rings whose equivalent depths (integrated product of normal optical depth and ring width) were ≥ 0.1 km (3, 26). At Neptune the slant optical depth measured by the PPS is 2.7 times higher than for an identical ring at Uranus because of the oblique viewing geometry, making relatively narrow lower optical depth rings easier to detect. However, the lower radial resolution of the Neptune occultation makes detection of narrow rings more difficult.

The σ Sgr occultation grazed the leading edge of one of the three imaging-detected bright regions located within ring 1989N1R (8) at a radial distance of about 63,000 km from the center of Neptune (Fig. 5). The PPS optical-depth profile of 1989N1R (Fig. 6) is characterized by a condensed core near the inner edge of the ring. A similar structure was observed in the 20 August 1985 occultation observed in Hawaii from the IRTF (Infrared Telescope Facility) and CFHT (Canadian, French, Hawaiian Telescope) observatories, but at this time the core appeared near the outer edge of the ring (27, 29). From the PPS data, the ring is about 50 kilometers in radial extent. At 1.5-km resolution, the normal optical depth of the core is about 0.05 with a width of 9 to 11 km. Outside the core the optical depth ranges from about 0.01 to 0.02. The entire ring as measured by the PPS has an equivalent depth of 0.78. The equivalent depths of the ground-based occultations are 1.30 to 2.15 km (27), which are approximately twice the value measured by the PPS. This is explained by the effects of diffraction (30) if the size of the particles is larger than a few centimeters.

A number of other features were observed at a lower level of significance, with the most interesting one near 53,000 km, close to the reported location of 1989N2R (8). This feature has an average normal optical depth of ~ 0.006 , a width of ~ 110 km, and an equivalent depth of about 0.7. Although such a feature could occur statistically four times in the total occultation data set, it is quite unlikely that it should appear by chance within 200 km of the reported location of 1989N2R. We are currently applying a variety of statistical techniques to the entire data set to elucidate other possible

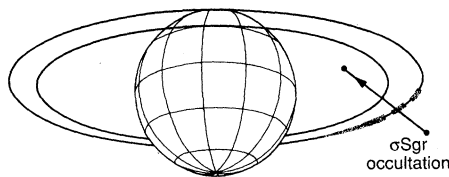


Fig. 5. Occultation geometry. The star σ Sagittarii passed through a portion of the Neptune ring system, ending in a nearly tangential occultation of the innermost region as viewed from Voyager as it approached Neptune. The star grazed the leading edge of one of the bright regions (ring arcs) in 1989N1R and also passed behind ring 1989N2R.

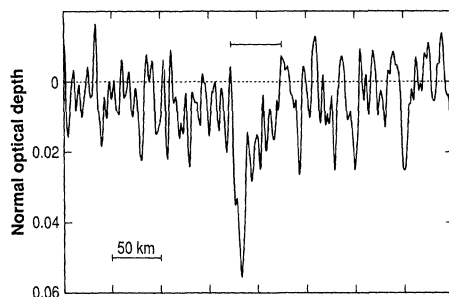


Fig. 6. View of 1989N1R. The optical depth profile of 1989N1R is shown. The “thickest” extent of the ring is indicated by the horizontal bar above the profile. The data for 1989N1R were smoothed to 1.5-km resolution.

regions of ring material.

The PPS profile of 1989N1R has strong similarities to our profile of the Saturnian F ring (2) and to the Uranian δ and η rings, with the radial profiles displaying a condensed core and adjacent wave-like oscillations (3, 26, 31). All of these rings exhibit a narrow core and have a broad, low-density companion. Azimuthally, both the F ring and the η ring are clumpy (32, 33), and the η ring varies by a factor of two in its equivalent width (26, 34). These variations have been attributed to nearby satellites. In the case of 1989N1R, a single satellite, 1989N4, was discovered by Voyager 2 (8) just interior to the orbit of 1989N1R.

Numerical simulations of the ring response to an isolated resonance from a nearby satellite show that the collisional response forms a sharp density enhancement at the resonance (35). The width of this sharp feature is approximately the width of the resonance that is given by the region in which the perturbed particles overlap: $w_0 \approx 1.8 a [M_s/M_p]^{1/2}$, where M_s and M_p are the satellite and planet masses, and a is the semi-major axis of the ring (36). For an isolated resonance from 1989N4, $w_0 \approx 20$ km, which is in reasonable agreement with the measured 9 to 11 km (above). A smaller, closer satellite than 1989N4 could also create this structure as long as its resonances are isolated. For example, an unseen moon with

radius 10 km must be more than 200 km from the ring. Brophy, Esposito, and Stewart (35) propose this mechanism to create the morphology of the Uranian δ ring, so the similarity of the δ ring core to the 1989N1R PPS profile is significant. The width and exact radial position should vary with azimuth, so comparisons with other data would be useful in testing this hypothesis. It is also possible that the satellites creating these resonances are also important in explaining the clumps seen in 1989N1R, similar to the phenomena simulated for the F ring by the work of Showalter and Burns (37) and Kolvoord and Burns (38).

If the Neptunian rings represent one part of a collisionally evolving system, as proposed by Esposito and Colwell (39) for the Uranian rings, we can compare the size distribution of material near Neptune to that near Uranus [fig. 1 in (39)]. Using the PPS measurements of equivalent depths, the measured sizes of the newly discovered satellites, and the reported optical depth and width of dusty rings (8), we find that the surface area in each of these components (dust, ring particles, 1989N2 through 1989N6, and 1989N1) is $\sim 10^{15}$ cm². This is consistent with these components being the observable part of a power-law size distribution with $q \approx 3$, where $n(a)da = C a^{-q}$, where da is the number of particles in the size interval $[a, a + da]$. However, since the size distribution of the ring particles is still unknown, this must be treated as a preliminary result (40). Further, without a measured size distribution, we cannot estimate the mass of the Neptunian rings. However, the total area of the Neptunian rings is about 1% of that of the Uranian rings, despite the fact that the amount of material in small moons near the ring is very similar in both systems. Thus we see that the Neptune ring system is markedly deficient in ring material by several orders of magnitude when compared to the Uranian ring system. One source of such material could be a moon-shattering event large enough to provide the amount of material such as that seen in the Uranian rings [2×10^{17} cm², figure 1 in (39)], which might imply that this kind of event has not happened as recently in the Neptunian system.

REFERENCES AND NOTES

1. C. W. Hord *et al.*, *Science* **206**, 956 (1979).
2. A. L. Lane *et al.*, *ibid.* **215**, 537 (1982).
3. A. L. Lane *et al.*, *ibid.* **233**, 65 (1986).
4. R. A. West *et al.*, in preparation.
5. J. Neff, personal communication.
6. J. Neff *et al.*, *Icarus* **60**, 221 (1984).
7. J. B. Pollack *et al.*, *J. Geophys. Res.* **92**, 15307 (1987).
8. B. A. Smith *et al.*, *Science* **246**, 1422 (1989).
9. L. P. Giver, *J. Quant. Spect. Rad. Transfer* **19**, 311 (1978).
10. H. B. Hammel, personal communication, based on

- the Mauna Kea observations of 24 August 1989.
11. K. H. Baines and W. H. Smith, in preparation.
 12. G. L. Tyler *et al.*, *Science* **246**, 1466 (1989).
 13. H. N. Russell, *Astrophys. J.* **43**, 173 (1916).
 14. Radii were based on information furnished by the Voyager Imaging Team in advance of publication (J. Gougen and P. Thomas, personal communication).
 15. R. M. Nelson *et al.*, *J. Geophys. Res.* **92**, 14905 (1987).
 16. B. W. Hapke, *Icarus* **67**, 264 (1986).
 17. B. J. Buratti and J. Veverka, *ibid.* **58**, 254 (1984).
 18. L. M. Trafton, in *Uranus and Neptune*, J. T. Bergstralh, Ed., NASA CP 2330, 481 (1984).
 19. J. Lunine and D. Stevenson, *Nature* **317**, 238 (1985).
 20. J. A. Stansberry, *Geophys. Res. Lett.* **16**, 961 (1989).
 21. A. P. Zent *et al.*, *ibid.*, p. 965.
 22. S. Stern, *ibid.*, p. 981.
 23. O. Franz, *Icarus* **45**, 602 (1981).
 24. N. Lark *et al.*, *ibid.* **79**, 239 (1989).
 25. B. J. Buratti and J. Veverka, *ibid.* **51**, 93 (1983).
 26. J. E. Colwell *et al.*, *ibid.*, in press.
 27. P. D. Nicholson *et al.*, in preparation.
 28. W. B. Hubbard *et al.*, *Nature* **319**, 636 (1986).
 29. C. E. Covault *et al.*, *Icarus* **67**, 126 (1986).
 30. J. N. Cuzzi, *ibid.* **63**, 312 (1985).
 31. L. J. Horn *et al.*, *ibid.* **76**, 485 (1988).
 32. B. A. Smith *et al.*, *Science* **212**, 163 (1981).
 33. B. A. Smith *et al.*, *ibid.* **233**, 43 (1986).
 34. R. G. French *et al.*, *Icarus* **67**, 134 (1986).
 35. T. G. Brophy, L. W. Esposito, G. R. Stewart, *Bull. Am. Astron. Soc.* **21**, 932 (1989).
 36. P. Goldreich and S. Tremaine, *Annu. Rev. Astron. Astrophys.* **20**, 249 (1982).
 37. M. R. Showalter and J. A. Burns, *Icarus* **52**, 526 (1982).
 38. R. A. Kolvoord and J. A. Burns, *Bull. Am. Astron. Soc.* **20**, 859 (1988).
 39. L. W. Esposito and J. Colwell, *Nature* **339**, 605 (1989).
 40. The Neptune pole used in the ring range calculations was right ascension = 298.7924°, declination = 42.8482°. The Voyager Navigation Team trajectory solution used was NAV K.I.
 41. With the completion of the Voyager 2 Grand Tour, the PPS Team acknowledges with heartfelt thanks all

the members of the Voyager Flight Team who worked so diligently to enable the PPS to have encounters with Jupiter, Saturn, Uranus, and Neptune, which were so filled with marvelous scientific results. To all those people, past and present, we owe a debt of immeasurable gratitude. The PPS team also remembers fondly J. Long and C. Stemberge, who, though no longer with us in body, were with us in spirit during this encounter. We also thank P. D. Nicholson and R. French for many helpful conversations as well as numerous geometry computations during the time period when each new pre-encounter satellite observation tweaked our knowledge of the Neptunian pole direction. The PPS team wishes to thank M. Morrison, S. Kuo, J. Hui, A. Graps, and B. Hapke for their help during the active Neptune encounter period. The continuing support of the NASA Office of Solar System Exploration is gratefully acknowledged. This work was support under NASA contracts to J.P.L. and the University of Colorado.

2 November 1989; accepted 15 November 1989

Infrared Observations of the Neptunian System

B. CONRATH, F. M. FLASAR, R. HANEL, V. KUNDE, W. MAGUIRE, J. PEARL, J. PIRRAGLIA, R. SAMUELSON, P. GIERASCH, A. WEIR, B. BEZARD, D. GAUTIER, D. CRUIKSHANK, L. HORN, R. SPRINGER, W. SHAFFER

The infrared interferometer spectrometer on Voyager 2 obtained thermal emission spectra of Neptune with a spectral resolution of 4.3 cm^{-1} . Measurements of reflected solar radiation were also obtained with a broadband radiometer sensitive in the visible and near infrared. Analysis of the strong C_2H_2 emission feature at 729 cm^{-1} suggests an acetylene mole fraction in the range between 9×10^{-8} and 9×10^{-7} . Vertical temperature profiles were derived between 30 and 1000 millibars at 70° and 42°S and 30°N . Temperature maps of the planet between 80°S and 30°N were obtained for two atmospheric layers, one in the lower stratosphere between 30 and 120 millibars and the other in the troposphere between 300 and 1000 millibars. Zonal mean temperatures obtained from these maps and from latitude scans indicate a relatively warm pole and equator with cooler mid-latitudes. This is qualitatively similar to the behavior found on Uranus even though the obliquities and internal heat fluxes of the two planets are markedly different. Comparison of winds derived from images with the vertical wind shear calculated from the temperature field indicates a general decay of wind speed with height, a phenomenon also observed on the other three giant planets. Strong, wavelike longitudinal thermal structure is found, some of which appears to be associated with the Great Dark Spot. An intense, localized cold region is seen in the lower stratosphere, which does not appear to be correlated with any visible feature. A preliminary estimate of the effective temperature of the planet yields a value of 59.3 ± 1.0 kelvins. Measurements of Triton provide an estimate of the daytime surface temperature of $38 \pm \frac{3}{4}$ kelvins.

DURING THE VOYAGER 2 ENCOUNTER, the infrared interferometer spectrometer (IRIS) obtained thermal emission and reflected solar radiation measurements of Neptune and Triton. The dual instrument consists of a Michelson

interferometer operating in the thermal infrared with a spectral resolution of 4.3 cm^{-1} and a single-channel radiometer sensitive to reflected sunlight between 0.4 and $1.5 \mu\text{m}$. Both components share a 50-cm Cassegrain telescope with a common circular field of

view of 0.25° full cone angle. The interferometer is calibrated by scaling the spectra of the observed object to that of deep space while maintaining the instrument at 200 K. Occasional measurements of reflected sunlight from a diffuse reflector carried on the spacecraft are used to calibrate the radiometer. The instrument and its characteristics have been described in detail elsewhere (1), and results obtained for the Jovian, Saturnian, and Uranian systems have been presented (2-6). In this report we describe preliminary results obtained for Neptune and Triton.

Thermal emission spectra of Neptune. Because of the very low temperatures encountered on Neptune, a signal-to-noise ratio greater than unity is achieved in individual spectra only in the spectral region between 200 and 320 cm^{-1} . Therefore, for most applications it is necessary to either use an average of several spectra or to integrate over broad intervals within individual spectra, or both. With this limitation in mind, observational sequences were designed and implemented that would provide adequate numbers of spectra to permit specific objectives to be met. Averages of several tens of spectra allow a useful effective signal-to-noise ratio to be achieved between 200 and 400 cm^{-1} , whereas averages of several hundred spectra permit analyses of selected spectral regions at higher wavenumbers to be carried out.

In Fig. 1 the spectrum corresponding to 70°S is an average of 390 individual spectra and that for 42°S is an average of 108 spectra. The Neptune spectrum over the wavenumber range shown is dominated by the $\text{S}(0)$ collision-induced absorption line of H_2 , which is centered at 354 cm^{-1} . The dominant factors that determine the behavior of the spectrum are the variation of atmospheric temperature with height and

B. Conrath, F. M. Flasar, R. Hanel, V. Kunde, W. Maguire, J. Pearl, J. Pirraglia, R. Samuelson, Laboratory for Extraterrestrial Physics, Goddard Space Flight Center, Greenbelt, MD 20771.
P. Gierasch and A. Weir, Astronomy Department, Cornell University, Ithaca, NY 14853.
B. Bezaud and D. Gautier, Paris Observatory, 92190

Meudon, France.
D. Cruikshank, Ames Research Center, Moffett Field, CA 94035.
L. Horn and R. Springer, Jet Propulsion Laboratory, Pasadena, CA 91109.
W. Shaffer, Department of Meteorology, University of Maryland, College Park, MD 20472.